Desalination and Water Treatment
www.deswater.com

doi: 10.5004/dwt.2022.28689

267 (2022) 283–292
August

Modification of $Co_3O_4/CuBi_2O_4$ composite for photocatalytic degradation of methylene blue dye

Punyanuch Thammaacheep[a], Kantapat Chansaenpak[b], Panatda Jannoey[c], Wilawan Khanitchaidecha[d,e], Auppatham Nakaruk[d,f], Duangdao Channei[a,*]

[a]*Department of Chemistry, Faculty of Science, Naresuan University, Phitsanulok 65000, Thailand, emails: duangdaoc@nu.ac.th (D. Channei), punyanuchth63@nu.ac.th (P. Thammaacheep)*
[b]*National Nanotechnology Center, National Science and Technology Development Agency, Thailand Science Park, Pathum Thani, 12120, email: kantapat.cha@nanotec.or.th (K. Chansaenpak)*
[c]*Department of Biochemistry, Faculty of Medical Science, Naresuan University, Phitsanulok 65000, Thailand, email: panatdaj@nu.ac.th (P. Jannoey)*
[d]*Centre of Excellence for Innovation and Technology for Water Treatment, Naresuan University, Phitsanulok 65000, Thailand, emails: wilawank@nu.ac.th (W. Khanitchaidecha), auppathamn@nu.ac.th (A. Nakaruk)*
[e]*Department of Civil Engineering, Faculty of Engineering, Naresuan University, Phitsanulok 65000, Thailand*
[f]*Department of Industrial Engineering, Faculty of Engineering, Naresuan University, Phitsanulok 65000, Thailand.*

Received 14 March 2022; Accepted 8 July 2022

ABSTRACT

Herein, we report the synthesis of cobalt oxide (Co_3O_4), copper bismuth oxide ($CuBi_2O_4$), and $Co_3O_4/CuBi_2O_4$ composite by a co-precipitation method. The effect of Co_3O_4 addition on phase composition and microstructure of $CuBi_2O_4$ is studied using X-ray diffraction, transmission electron microscopy, scanning electron microscopy-energy-dispersive X-ray spectroscopy. The surface area and pore structure have been studied by nitrogen adsorption–desorption isotherm based on Brunauer–Emmett–Teller theory. Optical properties of all photocatalysts are also investigated by diffuse reflectance spectra UV-Vis measurements. The intensity of photoluminescence is also used to measure the electron hole recombination in the unmodified Co_3O_4 and $CuBi_2O_4$ compared with the composite sample. The photocatalytic activities of the prepared samples are evaluated under visible light in the presence of the target pollutant, methylene blue (MB). The results show that coupling Co_3O_4 with $CuBi_2O_4$ could effectively promote photogenerated electron transfer in heterojunction, which is able to retard recombination process and thus improve their photocatalytic performance. In this system, $Co_3O_4/CuBi_2O_4$ exhibits the best photocatalytic activity in degrading 22% of MB within 120 min under visible irradiation. The apparent reaction rate constant (k) of the composite is 3.8 times greater than that of pure $CuBi_2O_4$, and around 1.3 time compared to pure Co_3O_4. Hence, the formation of a heterojunction between two photocatalysts is an efficient way to degrade the environmental pollutants in wastewater with the usage of photon energy, that can be further adapted for practical application.

Keywords: Cobalt oxide; Copper bismuth oxide; Composite materials; Photocatalysis

* Corresponding author.

1. Introduction

The problem of water pollution stems from the industrial wastewater. Due to the rapid expansion of the textile and garment industries, several fabric dyeing industries have been built leading to fast developments in both production processes and exports [1]. Water is the latter used in all processes such as fiber manufacturing, spinning, weaving, knitting, and dyeing. It needs to be treated properly to meet the effluent standards before releasing to the environment. Typically, textile industry-processing effluents contain dyes in the range between 10 and 200 mg/L. Most textile dyes can be detected at a rather low concentration of even < 1 mg/L by the human eye [2]. Therefore, treatment of wastewater from textile industry can be obtained by physical and chemical methods such as coagulation [3], electrochemical processes [4], adsorption [5], and microwave catalysis [6].

Even these methods are conventional approaches used to treat wastewater, they can generate secondary waste. The pollutant molecule is only adsorbed but not degraded to become less-toxic products. Thus, advanced oxidation process (AOP) for photocatalytic contaminant degradation using photocatalyst is an alternative method to help remove these contaminants in the traditional wastewater treatment system since it can mineralize the pollutants by redox reactions to less toxic compounds [7–10]. The mechanism of photocatalysis in oxidizing organic compounds in water can be classified into three main steps:

- e^-/h^+ pairs are generated on the surface of semiconductor photocatalyst under light irradiation with the required photon energy equal to or higher than the band gap energy level.

$$\text{Photocatalyst + photon energy} \rightarrow \text{Photocatalyst } (e^-_{CB} + h^+_{VB})$$

- photogenerated charges (e^-/h^+) migrate to the surface of the photocatalyst.
- e^- and h^+ induce redox reactions on the surface that facilitate destruction of organic pollutants.

$$h^+_{VB} + H_2O \rightarrow H^+ + OH^\bullet \quad \text{(valence band)}$$

$$h^+_{VB} + OH^- \rightarrow OH^\bullet \quad \text{(valence band)}$$

$$e^-_{CB} + O_2 \rightarrow O_2^{\bullet -} \quad \text{(conduction band)}$$

$$O_2^{\bullet -} + H_2O \rightarrow 2OH^\bullet \quad \text{(conduction band)}$$

$$OH^\bullet + \text{Pollutant (dye)} \rightarrow CO_2 + H_2O + \text{small molecules}$$

Among the several metal oxide photocatalysts, cobalt oxide (Co_3O_4) has been recognized as one of the promising photocatalyst materials for photo-degradation under visible light. The spinel cobalt oxide Co3O4 is a p-type semiconductor containing cobalt ions in Co^{2+} and Co^{3+} oxidation states. The mixed valence states of Co3O4 are very helpful in redox reactions for dye degradation by photo-Fenton reaction [11]. Because of its relatively narrow band gap (1.48–2.19 eV), Co_3O_4 can be activated by visible light and natural sunlight, which challenges in practical application [12]. In addition, low photocatalytic activity is shown for Co_3O_4 due to its narrow band gap, which correlates to the rapid recombination of electron–hole pairs.

There are two common methods applied to modify the visible-light-active Co_3O_4: (i) doping with metal/nonmetal elements and (ii) forming heterojunction semiconductors [13]. Fabricating heterostructures is one of effective strategy for improving the photocatalytic performance of Co_3O_4 photocatalyst. Compared with the single Co_3O_4, the coupling system can bring a series of formations and functions.

Some photocatalysts presented in literature including $BiVO_4$ [14], ZnO [15], CdS [16], and TiO_2 [17] were selected as photocatalyst materials to combine with Co_3O_4. These composites exhibited high performance toward the degradation of dye pollutants, CO_2 reduction, and benzene oxidation.

Long et al. [14] summarized the design p-n heterojunction semiconductor $Co_3O_4/BiVO_4$, and applications of heterostructures for phenol degradation under visible light irradiation. The results showed that optimum addition of 5% Co_3O_4 with 95% $BiVO_4$ enhanced the degradation of phenol by 30.1% in 180 min. Li et al. [15] fabricated a hollow structured p-n heterojunction catalyst, polydopamine (PDA)-ZnO/Co_3O_4 and tested it for photocatalytic CO_2 reduction. The resulting PDA-modified ZnO/Co_3O_4 composites exhibited an impressive CO_2 reduction. Yang et al. [16] reported the heterostructure of Co_3O_4@CdS hollow spheres with the synergistic effects on the photocatalytic activities through phenol and dye degradation. The Co_3O_4@CdS composites with the assistance of the zeolitic imidazolate frameworks (ZIF-67) exhibited the highest photodegradation activity. Approximately, 90% phenol was degraded after 2 h of visible-light irradiation. In the first 30 min, RhB dye was degraded by almost 70% and completely degraded in 1 h of irradiation. Shi et al. [17] chemically assembled Co_3O_4/TiO_2 nanocomposites to achieve higher efficiency of light-driven thermocatalytic benzene oxidation under UV-Vis infrared irradiation. The optimum Co_3O_4/TiO_2 nanocomposite (Co/Ti molar ratio, 0.3) showed excellent durability for benzene reduction and caused a great enhancement of 489 times in benzene mineralization rate.

In addition, bismuth-containing materials such as visible-light-active $BiVO_4$, Bi_2O_3, BiOI, and $CuBi_2O_4$ displayed better activities than the photocatalyst with single component [18–21]. Among various narrow band gap semiconductors, the AB_2O_4 spinel type such as copper bismuth oxide ($CuBi_2O_4$) is an attractive material for the photo-oxidation of pollutants because of its suitable band gap and diverse crystal structures [22,23]. $CuBi_2O_4$ is a p-type semiconductor material with a low band gap (1.5–1.8 eV) that is ideal for use in photocatalytic processes when exposed to visible light [21–23].

In a typical heterojunction, the type II band alignment (staggered gap) offers the best charge separation because the relative positions of the valence and conduction bands allow the mobility of electrons from the conduction band of photocatalyst A to that of photocatalyst B [24]. Herein, for matched band alignment, $CuBi_2O_4$ have been chosen to form heterojunction with Co_3O_4 as the potentials of conduction

band (CB) and valence band (VB) edges of these two materials are expected to favor for charge transfer. Structural, morphological, surface, and optical characterizations of the composites compared to the pure photocatalyst were fully characterized. The photocatalytic degradation mechanism for MB degradation under visible light irritation were also proposed.

2. Experimental

All the start materials were used as received from authentic companies without further purification. Herein, cobalt(II) acetate tetrahydrate, citric acid, copper(II) nitrate trihydrate, bismuth(III) nitrate pentahydrate, ethylene glycol (EG), isopropanol, sodium hydroxide, and distilled water were used for the preparation of the photocatalysts.

2.1. Preparation of cobalt oxide (Co_3O_4)

Co_3O_4 was prepared by co-precipitation method. Typically, cobalt(II) acetate tetrahydrate (0.05 M) was dissolved in 60 mL ethylene glycol under vigorous magnetic stirring. Citric acid was dissolved in 60 mL isopropanol under vigorous magnetic stirring. Then, the citric acid solution was slowly added dropwise to cobalt(II) acetate solution under continuous stirring for 30 min to form a homogeneous solution. Next, 0.1 M NaOH (100 mL), the precipitating agent, was added dropwise into the mixture under continuous stirring for 6 h at 60°C. The precipitate was filtered using centrifugation machine (5,000 rpm, 5 min), washed with DI water for several times, and dried at 100°C for 12 h in a hot air oven. Finally, the black powder of Co_3O_4 was obtained after calcination at 600°C for 2 h.

2.2. Preparation of copper bismuth oxide ($CuBi_2O_4$)

In a typical experiment, copper(II) nitrate trihydrate (0.05 M) and bismuth(III) nitrate pentahydrate (0.05 M) was dissolved separately in 25 mL DI water with continuous stirring for 30 min [21]. All mixed solutions were adjusted to a constant pH value of 14 by 2 M NaOH and further stirred for 10 h. The filtered powders were washed and dried at 100°C for 2 h. The obtained $CuBi_2O_4$ powders were then calcined at 600°C for 3 h.

2.3. Preparation of $Co_3O_4/CuBi_2O_4$ composites

$Co_3O_4/CuBi_2O_4$ composite heterojunction was prepared with the mass ratio of 1:1. Before adjusting the pH value of the mixture to 14, different amounts of Co_3O_4 powders were added to the above solution. The Co_3O_4 particles were kept dispersed in the mixed suspensions and stirred for 10 h at room temperature. After stirring, the $Co_3O_4/CuBi_2O_4$ composites were collected, washed and dried at 100°C for 2 h, respectively. Finally, the produced $Co_3O_4/CuBi_2O_4$ composites were calcined at 600°C for 3 h, as shown in Fig. 1.

2.4. Material characterizations

Crystallographic structures and phase composition were detected by an X-ray diffraction instrument (XRD, Philips X'PERT MPD). The morphologies were studied using field-emission scanning electron microscope (FESEM, HITACHI SU-8030, Japan) equipped with energy-dispersive X-ray spectrometer (EDS) for elemental analysis. Transmission electron microscopic (TEM) images were acquired from a JEM-2100 Plus transmission electron microscope (JEOL JEM-2100, Japan). The specific surface area was determined from N_2 adsorption/desorption isotherms based on the Brunauer–Emmett–Teller (BET) theory (Micromeritics TriStar II 3020, USA). The photoluminescence (PL) benchtop spectrophotometer excited with a 350 nm light source was used for analyzing the emission wavelength (HORIBA Jobin Yvon FluoroMax-4, France). Optical studies for reflectance, absorbance and band gap analysis were analyzed using diffuse reflectance spectra (DRS) on a UV-Vis spectrophotometer (Shimadzu UV-3101PC).

2.5. Photocatalytic degradation

The photocatalytic activities were conducted by adding 0.05 g of the prepared photocatalysts into 50 mL of 3 ppm (C_0) methylene blue (MB) solution. Before light irradiation, the solution was stirred for 30 min in the dark. Under visible light irradiation, the photocatalytic degradation of MB was studied in home-made photoreactor combined with 18 W halogen lamp. The MB solution was collected every 30 min (0, 30, 60, 90, and 120 min) under light irradiation. The remaining concentration of MB dye in solution (C_t) at the wavelength of 664 nm was evaluated using a double beam UV-Visible spectrophotometer (Shanghai Mapada Instruments Co., Ltd.). The absorbance (A) of the MB solution is then converted to the remaining concentration (C_t) using the equation for the standard curve (Beer Lambert Law). A linear calibration curve was conducted by preparing a series of known MB concentrations (0, 1, 2, 3, 4, and 5 ppm).

In the part of hydroxyl radical trapping, terephthalic acid (TA) was used as trapping reagent. This method is based on the fluorescent properties of hydroxyterephthalic acid (TAOH). Typically, 0.05 g of photocatalyst was added in 200 mL of a 0.5 mM TA aqueous solution containing 2 mM NaOH as a solvent and continued stirring for 30 min in the dark. After that, the level of hydroxyl radicals were subjected to generate in the reaction system under visible light irradiation. The suspension was then centrifuged, and the fluorescence intensity in the supernatant solution was measured at 425 nm with the excitation wavelength at 315 nm (Fluoromax-4 Horiba Jobin Yvon).

3. Results and discussion

The XRD characterization method was used to investigate the crystal phases, crystallinity degree, crystal sizes, and phase purity of the prepared photocatalysts [25]. The XRD patterns of conventional Co_3O_4, standard $CuBi_2O_4$, and synthetic $Co_3O_4/CuBi_2O_4$ heterojunction are presented in Fig. 2. The diffraction peaks of $CuBi_2O_4$ were consistent with the tetragonal phase (space group P4/ncc) (JCPDS no. 00-42-0334) [26]. The main diffraction peaks of Co_3O_4 corresponded to a cubic form in the Fd-3m space group (JCPDS no. 01-073-1701) [27]. There were no additional peaks present in the XRD patterns. In the case of

$Co_3O_4/CuBi_2O_4$ composite, a mixture of cubic Co_3O_4 and tetragonal $CuBi_2O_4$ phase was observed from the sharp characteristic peaks.

The scanning electron microscopy (SEM) and TEM characterization techniques were used to investigate and characterize the shape, size, crystallinity degree, and composition state of bare Co_3O_4, $CuBi_2O_4$, and $Co_3O_4/CuBi_2O_4$ composites. As shown in Fig. 3, SEM images of Co_3O_4 showed a spherical morphology with an irregular particle size of roughly 0.15 μm (Fig. 3a), while sheet-like form with a length of approximately 0.76 μm was found SEM images of $CuBi_2O_4$ (Fig. 3b). According to the $Co_3O_4/CuBi_2O_4$ SEM image, the as-synthesized $Co_3O_4/CuBi_2O_4$ composite exhibited a well-defined combination of Co_3O_4 and $CuBi_2O_4$ phases by the dispersion of Co_3O_4 particles supported on the $CuBi_2O_4$ surface (Fig. 3c). As shown in Fig. 3d, EDS result displayed that $Co_3O_4/CuBi_2O_4$ mainly contained Co, Cu, Bi, and O elements. In the EDS result, the appearance of high intensity between 1–2 KeV can be related to the coated Au for SEM analysis. In the case of TEM analysis, the Co_3O_4 sample consisted of aggregated spherical particles with the broad size less than 100 nm as displayed in Fig. 4a. In addition, Fig. 4b confirmed the rod-shaped and plate-like morphology of $CuBi_2O_4$. In Fig. 4c, mixed morphology of two materials was observed in composite sample, which revealed the dispersion of small Co_3O_4 particles in $CuBi_2O_4$ medium.

The N_2 adsorption–desorption isotherms of the as-synthesized Co_3O_4, $CuBi_2O_4$, and $Co_3O_4/CuBi_2O_4$ composite were also investigated to study porosity of the materials. It was observed that the curve of composite was similar to that of bare $CuBi_2O_4$ and Co_3O_4 (Fig. 5a). During the progress of adsorption, desorption was enhanced with hysteresis loop, which was a typical characteristic of the type IV isotherm adsorption curve with mesoporous (2 nm < pore size < 50 nm) [28]. It can be seen from the Table 1 that the pore sizes of all samples were basically distributed in 4.41–4.83 nm, indicating that the as-synthesized photocatalysts were mesoporous materials. This is associated with the pore size distribution calculated by Barrett–Joyner–Halenda (BJH) method [29]. As shown in Fig. 5b, pore size distributions of all samples, calculated by the BJH analysis, are relatively narrow and center at around 2 and 10 nm which are in accordance with characteristic of mesoporous material according to IUPAC classification [30]. The specific surface area and the pore volume of composite sample (5.00 m^2/g and 0.0052 cm^3/g) were slightly higher than that of bare samples, which may be beneficial for enhancing the photocatalytic activities due to more reaction active sites during the photocatalytic process.

The optical properties including reflectance spectra (R), absorption characteristics and band gap of the samples are shown in Fig. 6. Firstly, the solid samples were analyzed in term of UV-Vis diffuse reflectance spectra (DRS), as shown in Fig. 6a. Then the absorption data was calculated from the Kubelka–Munk function, F(R), as a function wavelength

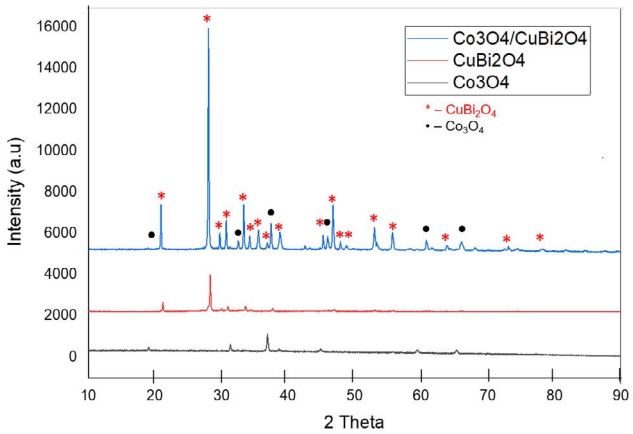

Fig. 2. XRD patterns of Co_3O_4, $CuBi_2O_4$ and $Co_3O_4/CuBi_2O_4$ composite.

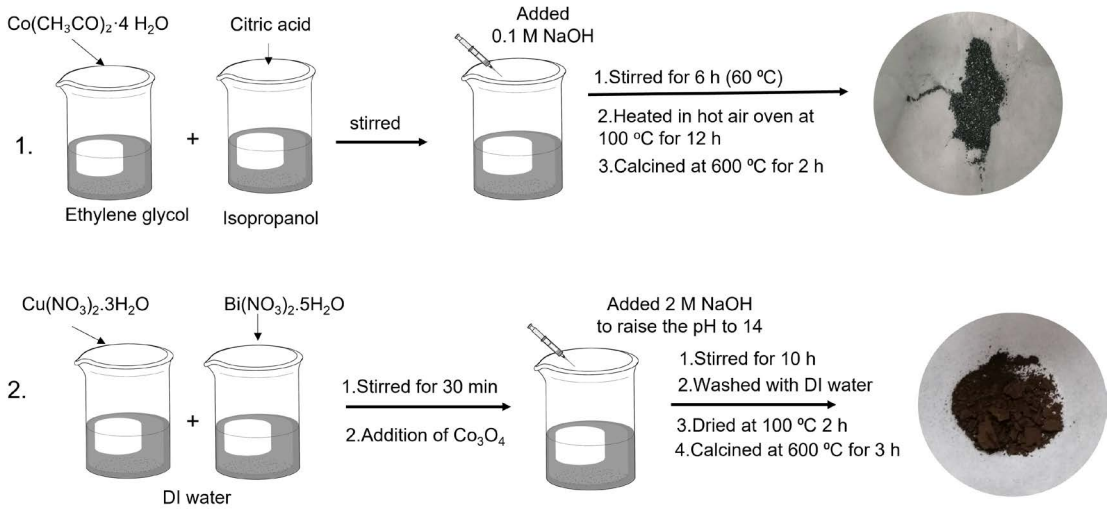

Fig. 1. Schematic representation for the preparation of $Co_3O_4/CuBi_2O_4$ composite.

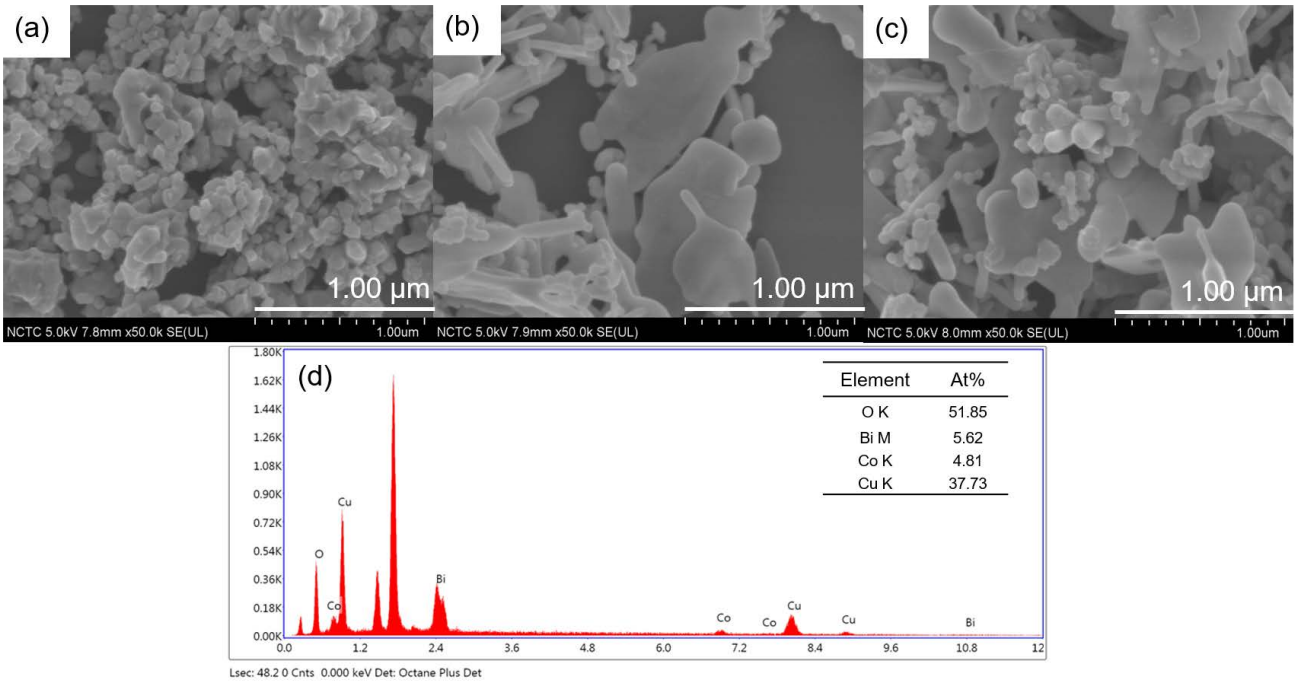

Fig. 3. SEM images of (a) Co_3O_4, (b) $CuBi_2O_4$, (c) $Co_3O_4/CuBi_2O_4$, and (d) EDS diagram of $Co_3O_4/CuBi_2O_4$

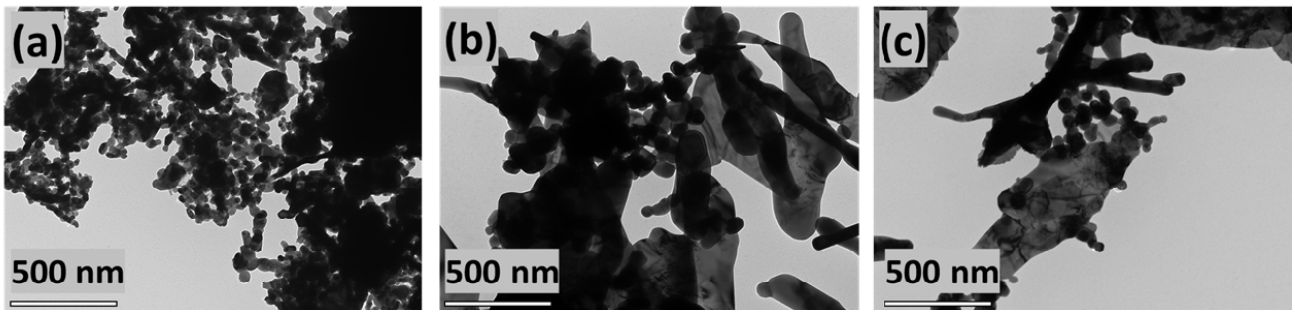

Fig. 4. TEM images of (a) Co_3O_4, (b) $CuBi_2O_4$, and (c) $Co_3O_4/CuBi_2O_4$.

Table 1
Specific surface area, pore volume and pore size

Samples	Specific surface area (m^2/g)	Pore volume (cm^3/g)	Pore size distribution (nm)
Co_3O_4	4.54	0.0039	4.83
$CuBi_2O_4$	4.43	0.0040	4.51
$Co_3O_4/CuBi_2O_4$	5.00	0.0052	4.41

derived from the measured diffuse reflectance spectra (R). It can be written in the following form;

$$F(R) = \frac{(1-R)^2}{2R} \quad (1)$$

As shown in Fig. 6b, all samples had a strong absorption at wavelength above 400 nm, confirming its beneficial light response in the visible area that can lead to reactivity under visible light. A Tauc plots ($[F(R)h\nu]^2$ vs. photon energy ($h\nu$) were then obtained in Fig. 6c. The band gap (E_g) was determined from the extrapolation of the linear fit for the Tauc plot to the x-axis [31]. It was estimated that E_g values of the bare Co_3O_4 and $CuBi_2O_4$ were 2.0 and 2.7 eV, respectively. The band gap of the composite sample was calculated as 2.5 eV, which was closed to the value of $CuBi_2O_4$ host material.

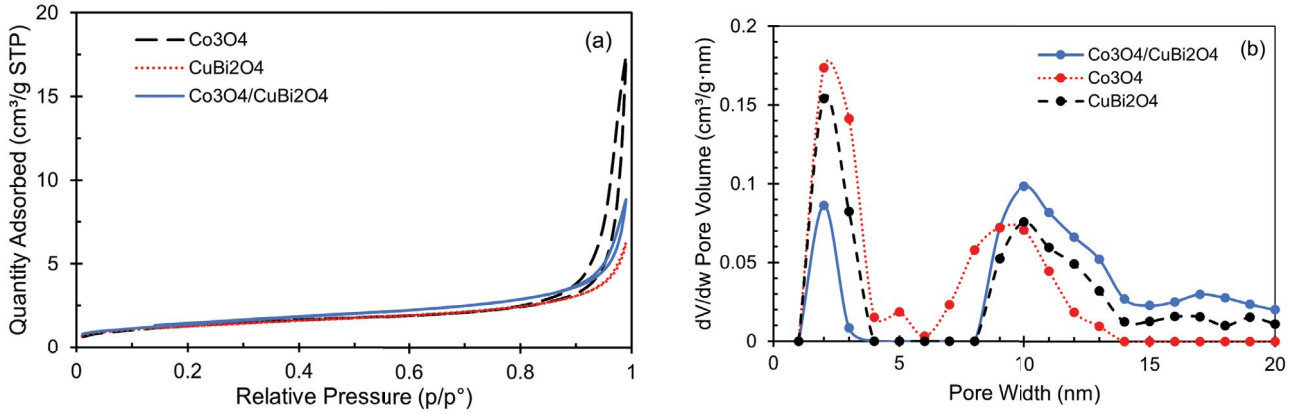

Fig. 5. (a) The N_2 adsorption–desorption isotherms and (b) the pore size distribution by BJH method.

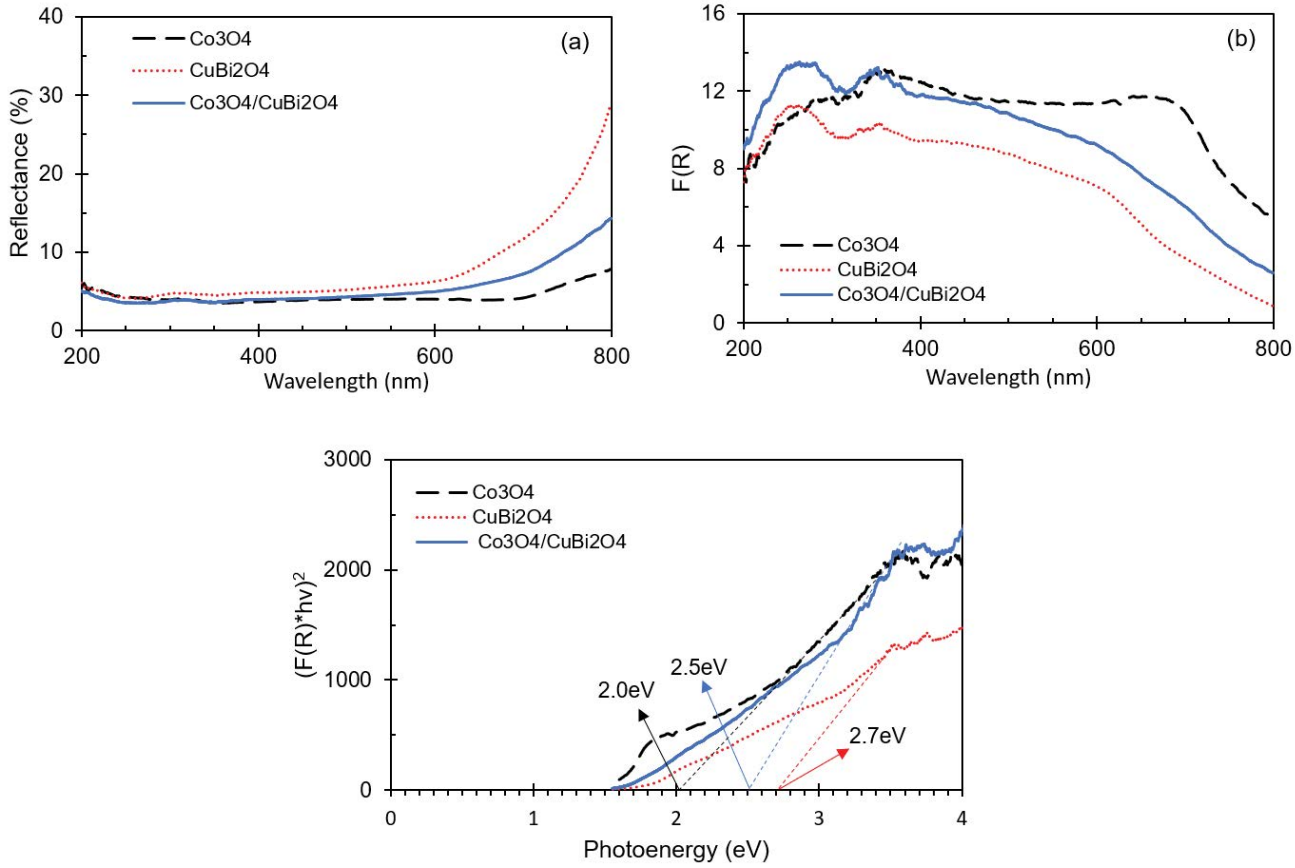

Fig. 6. (a) UV-Vis diffuse reflectance spectra, (b) Kubelka–Munk absorbance spectra, and (c) band gap estimation according to Tauc's model.

The efficiencies of photoexcited charge transfer, immigration, trapping, and electron–hole recombination of the prepared samples were investigated using photoluminescence. In general, the lower the PL intensity, the lower the recombination rate, and the higher the photocatalytic activity. As shown in Fig. 7, the PL emission intensity of $Co_3O_4/CuBi_2O_4$ composite was lower than that of bare Co_3O_4 and $CuBi_2O_4$ samples, suggesting that the charge carriers (electron and hole) were trapped by the electron–hole transfer on the heterojunction, leading to enhancing the charge separation efficiency.

The photocatalytic degradation of MB dyes was investigated in the presence of Co_3O_4, $CuBi_2O_4$, and $Co_3O_4/CuBi_2O_4$ composite. The percentage of MB photocatalytic degradation was investigated as a function of visible light irradiation time as shown in Fig. 8a. The results indicated that making composite materials can enhance the photocatalytic performance. The un-doped Co_3O_4 and

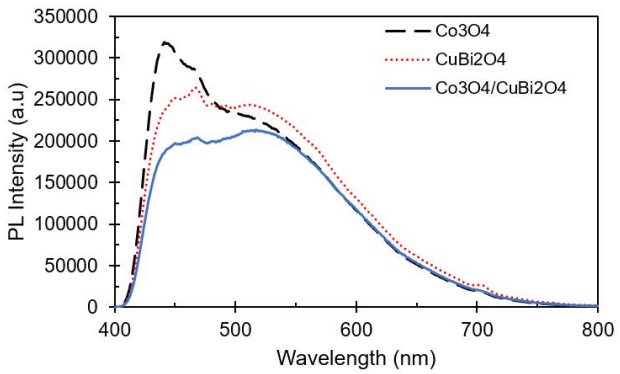

Fig. 7. PL spectra of bare Co_3O_4, $CuBi_2O_4$ and $Co_3O_4/CuBi_2O_4$ composite.

Table 2
Calculation of the CB and VB potentials of Co_3O_4 and $CuBi_2O_4$

Sample	χ	E_g (eV)	E_{CB} (eV)	E_{VB} (eV)
Co_3O_4	5.90	2.0	0.40	2.40
$CuBi_2O_4$	4.59	2.7	–1.26	1.44

$CuBi_2O_4$ showed only ~1% MB dark adsorption, while $Co_3O_4/CuBi_2O_4$ composite exhibited ~3% of MB dark adsorption which related to the specific surface area from BET study. Under the visible irradiation, $Co_3O_4/CuBi_2O_4$ composite shows better photocatalytic performance (22%) than that of bare Co_3O_4 (16%) and $CuBi_2O_4$ (7.5%) after 120 min irradiation.

The kinetics plot for of the MB photodegradation was found to be pseudo-first-order kinetics, as shown in the following equation [32,33]; where C_o is the initial MB concentration and C_t refers to the concentration of remaining MB.

$$-\ln\frac{C_t}{C_o} = k_t \tag{2}$$

The slope of the linear fit gives the rate constant (k, min^{-1}) of the degradation process. As seen in Fig. 8b, the composite catalyst displayed rate constants of 0.0031 min^{-1} which was 3.8 and 1.3 times higher than of bare $CuBi_2O_4$ (0.0008 min^{-1}) and Co_3O_4 (0.0011 min^{-1}), respectively. This better photocatalytic activity can be explained by electron transfer through $Co_3O_4/CuBi_2O_4$ heterojunction working under visible light.

The VB and CB edge position of semiconductor are estimated from the electronegativity [34] and experimental band gap values using the following relation:

$$E_{CB} = E_{VB} - E_g \tag{3}$$

$$E_{CB} = \chi - 4.5 + 0.5E_g \tag{4}$$

where χ is the absolute electronegativity (5.90 eV for Co_3O_4 and 4.59 eV for $CuBi_2O_4$) [35,36], E_g is the estimated band gap energy of Co_3O_4 and $CuBi_2O_4$ from this study (2.0 and 2.7 eV), E_{VB} and E_{CB} are the valence band edge and conduction band edge, respectively. The calculated values of the CB and VB potentials of Co_3O_4 and $CuBi_2O_4$ are listed in Table 2.

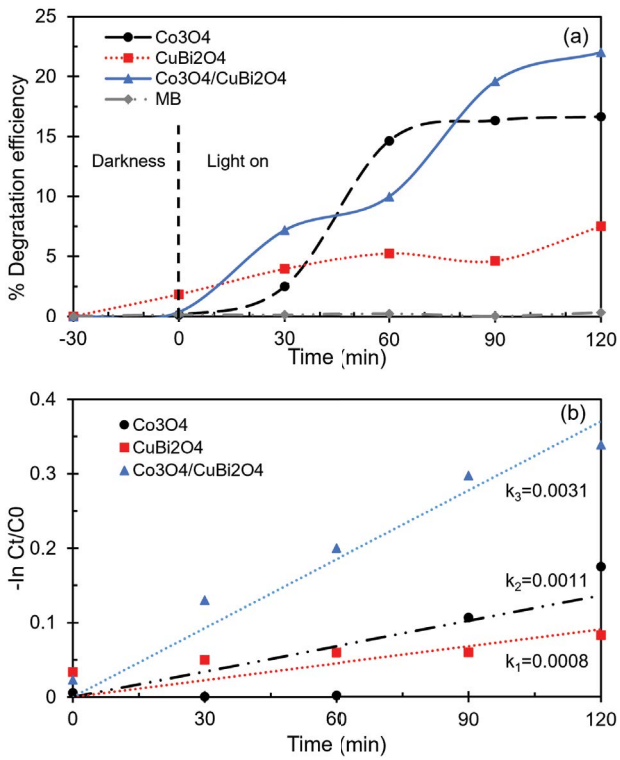

Fig. 8. (a) Photocatalytic degradation efficiency over different photocatalysts and (b) pseudo-first-order kinetic plot.

The possible photodegradation mechanism and band structure of the $Co_3O_4/CuBi_2O_4$ heterojunction is proposed in Fig. 9a. The matching band potentials between two semiconductors are recognized to be the driving factor for charge transfer. According to the valence band (VB) and conduction band (CB) potentials of $CuBi_2O_4$ (1.44 and –1.26 eV, respectively) and those of Co_3O_4 (2.40 and 0.40 eV, respectively) reported in this study, the prepared composites provide matching energy band structures as type II band alignments (staggered band gap).

Under visible-light illumination, both Co_3O_4 and $CuBi_2O_4$ are photoexcited to generate electrons and holes. These photogenerated electrons on the CB of $CuBi_2O_4$ migrate from $CuBi_2O_4$ with a higher CB position to Co_3O_4, which has a lower CB position, and could effectively react with O_2 adsorbed on the surface of $CuBi_2O_4$ to produce superoxide radicals (O_2^-). Then, the superoxide radicals are turned into hydroxyl radicals (•OH). After that, hydroxyl radicals could finally react with MB molecule adsorbed on the photocatalyst surface. The hydroxyl radicals as active species can react directly with MB molecules on the photocatalyst surface to decolorize the MB dye, and the small molecules can be mineralized to form CO_2, H_2O [37]. Since the VB position (1.44 eV) of $CuBi_2O_4$ is less than the VB position of Co_3O_4 (2.40 eV), the photogenerated holes

in the VB of Co_3O_4 will move to the VB of $CuBi_2O_4$ to reacts with surface bound H_2O to produce hydroxyl radicals. In this case, Co_3O_4 acted as an electron sink and $CuBi_2O_4$ behaved as a hole sink. Therefore, an effective charge separation of electron and hole could be achieved, resulting in enhancement of photocatalytic activity in the composite sample. To confirm the presence of the hydroxyl radicals ($OH^{\bullet}$) generated in the catalytic process, the terephthalic acid (TA), the non-fluorescent substance, was utilized to react with $OH^{\bullet}$ yielding 2-hydroxyterephthalic acid (TAOH) as the fluorescent product [38,39]. The fluorescence intensity of TAOH at 425 nm can be related to the amount of the $OH^{\bullet}$ generation. Fig. 9b shows time-dependent fluorescence emission TAOH solutions generated by Co_3O_4/$CuBi_2O_4$ under visible-light irradiation. The PL intensities of TAOH at 425 nm steadily increased with the increased irradiation time from 60 to 120 min. Therefore, this result confirmed that the amount of $OH^{\bullet}$ generated upon light irradiation was directly proportional to the irradiation time.

4. Conclusion

In conclusion, the Co_3O_4/$CuBi_2O_4$ heterojunction was successfully prepared using the co-precipitation method. The photocatalytic degradation of MB over Co_3O_4, and $CuBi_2O_4$ compared to Co_3O_4/$CuBi_2O_4$ composite was summarized in this paper. Co_3O_4/$CuBi_2O_4$ composite exhibited the greatest photodegradation efficiency among the studied materials.

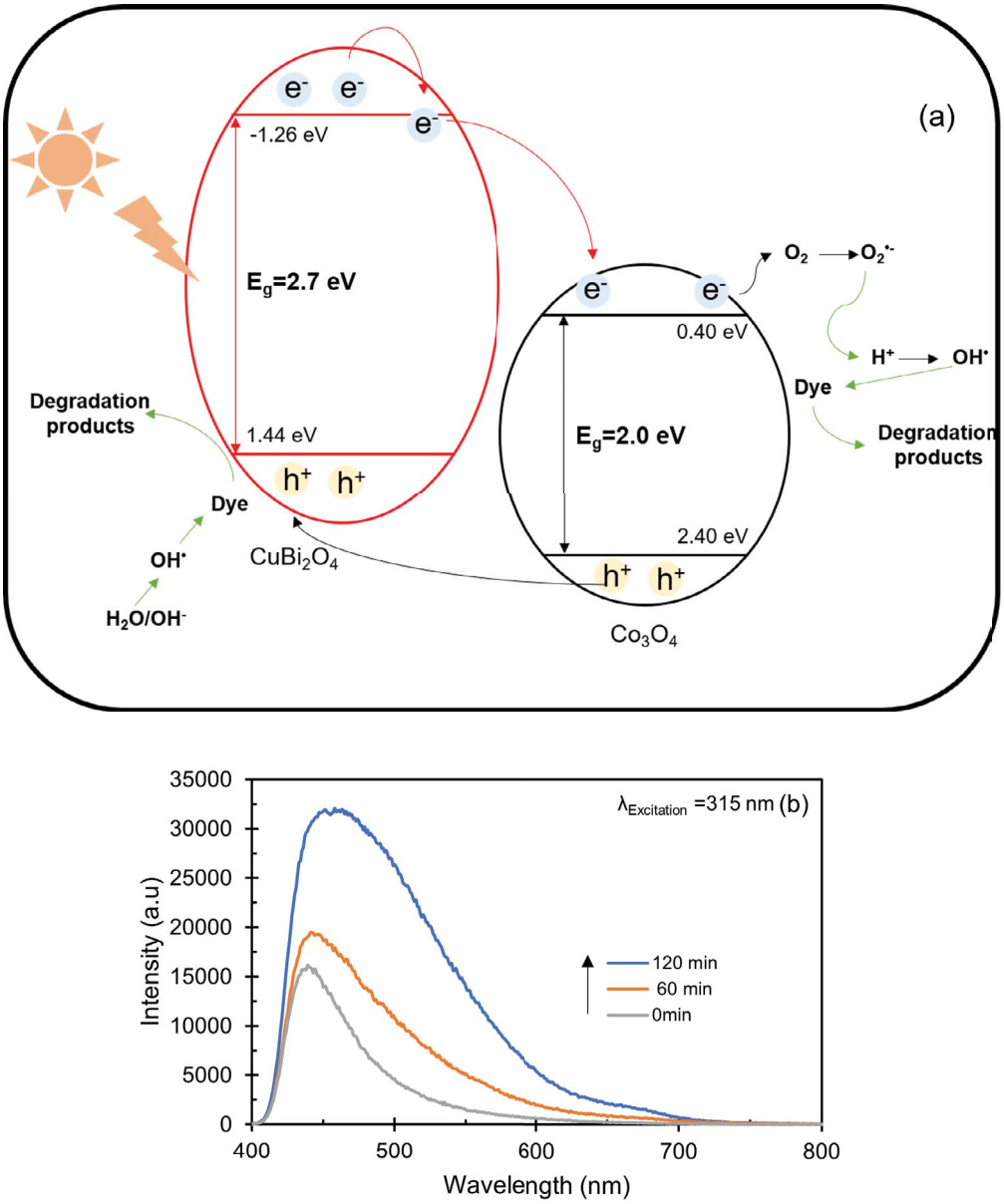

Fig. 9. (a) Schematic of photocatalytic reaction over the composite and (b) fluorescence spectra of TAOH solutions generated by Co_3O_4/$CuBi_2O_4$ composite.

The higher photocatalytic performance of the $Co_3O_4/CuBi_2O_4$ composite could be the result from the synergistic impact of Co_3O_4 and $CuBi_2O_4$ as the formation of heterojunctions of the two materials led to the efficient separation of electron–hole pairs that could retard electron–hole recombination. The conversion of TA to TAOH confirmed the $OH^{\bullet}$ generation through photocatalysis reaction which indicated the successful transfer of photogenerated charge carriers and separation. Finally, this work provided an idea for modification strategies to design optimized composite systems with better photocatalytic performance for future environmental applications.

Acknowledgments

This research was financially supported by Thailand Graduate Institute of Science and Technology, TGIST (Grant no. SCA-CO-2563-12179-TH/2563).

References

[1] K.-I. Choi, H.-R. Kim, K.-M. Kim, D. Liu, G. Cao, J.-H. Lee, C_2H_5OH sensing characteristics of various Co_3O_4 nanostructures prepared by solvothermal reaction, Sens. Actuators, B, 146 (2010) 183–189.

[2] C. Lavanya, R. Dhankar, S. Chhikara, S. Sheoran, Degradation of toxic dyes: a review, Int. J. Curr. Microbiol. Appl. Sci., 3 (2014) 189–199.

[3] J.-Q. Jiang, The role of coagulation in water treatment, Curr. Opin. Chem. Eng., 8 (2015) 36–44.

[4] Y. Tan, J. Kan, S. Li, Amperometric biosensor for catechol using electrochemical template process, Sens. Actuators, B, 152 (2011) 285–291.

[5] Z. Zhu, R. Rao, Z. Zhao, J. Chen, W. Jiang, F. Bi, Y. Yang, X. Zhang, Research progress on removal of phthalates pollutants from environment, J. Mol. Liq., 355 (2022) 118930, doi: 10.1016/j.molliq.2022.118930.

[6] Y. Wang, R. Wang, N. Lin, J. Xu, X. Liu, N. Liu, X. Zhang, Degradation of norfloxacin by MOF-derived lamellar carbon nanocomposites based on microwave-driven Fenton reaction: improved Fe(III)/Fe(II) cycle, Chemosphere, 293 (2022) 133614, doi: 10.1016/j.chemosphere.2022.133614.

[7] Y. Gong, Y. Wang, N. Lin, R. Wang, M. Wang, X. Zhang, Iron-based materials for simultaneous removal of heavy metal(loid)s and emerging organic contaminants from the aquatic environment: recent advances and perspectives, Environ. Pollut., 299 (2022) 118871, doi: 10.1016/j.envpol.2022.118871.

[8] N. Lin, Y. Gong, R. Wang, Y. Wang, X. Zhang, Critical review of perovskite-based materials in advanced oxidation system for wastewater treatment: design, applications and mechanisms, J. Hazard. Mater., 424 (2022) 127637, doi: 10.1016/j.jhazmat.2021.127637.

[9] A. Akhundi, A. Badiei, G.M. Ziarani, A. Habibi-Yangjeh, M.J. Muñoz-Batista, R. Luque, Graphitic carbon nitride-based photocatalysts: toward efficient organic transformation for value-added chemicals production, Mol. Catal., 488 (2020) 110902(1–14), doi: 10.1016/j.mcat.2020.110902.

[10] S. Asadzadeh-Khaneghah, A. Habibi-Yangjeh, g-C_3N_4/carbon dot-based nanocomposites serve as efficacious photocatalysts for environmental purification and energy generation: a review, J. Cleaner Prod., 276 (2020) 124319(1–19), doi: 10.1016/j.jclepro.2020.124319.

[11] T. Warang, N. Patel, R. Fernandes, N. Bazzanella, A. Miotello, Co_3O_4 nanoparticles assembled coatings synthesized by different techniques for photo-degradation of methylene blue dye, Appl. Catal., B, 132–133 (2013) 204–211.

[12] W. Chen, B. Han, C. Tian, X. Liu, S. Liang, H. Deng, Z. Lin, MOFs-derived ultrathin holey Co_3O_4 nanosheets for enhanced visible light CO_2 reduction, Appl. Catal., B, 244 (2019) 996–1003.

[13] M. Liang, M. Zhao, H. Wang, F. Wang, X. Song, Excellent cycling stabilities of a novel calliandra-like Co_3O_4 acted as anode materials for the lithium-ion battery, J. Energy Storage, 17 (2018) 311–317.

[14] M. Long, W. Cai, J. Jun, B. Zhou, X. Chai, Y. Wu, Efficient photocatalytic degradation of phenol over $Co_3O_4/BiVO_4$ composite under visible light irradiation, J. Phys. Chem. B, 110 (2006) 20211–20216.

[15] M. Li, S. Zhang, L. Li, J. Han, X. Zhu, Q. Ge, H. Wang, Construction of highly active and selective polydopamine modified hollow ZnO/Co_3O_4 p-n heterojunction catalyst for photocatalytic CO_2 reduction, ACS Sustainable Chem. Eng., 8 (2020) 11465–11476.

[16] H. Yang, J. Fan, C. Zhou, R. Luo, H. Liu, Y. Wan, J. Zhang, J. Chen, G. Wang, R. Wang, C. Jiang, Co_3O_4@CdS hollow spheres derived from ZIF-67 with a high phenol and dye photodegradation activity, ACS Omega, 5 (2020) 17160–17169.

[17] Z. Shi, L. Lan, Y. Li, Y. Yang, Q. Zhang, J. Wu, G. Zhang, X. Zhao, Co_3O_4/TiO_2 nanocomposite formation leads to improvement in ultraviolet–visible-infrared-driven thermocatalytic activity due to photoactivation and photocatalysis–thermocatalysis synergetic effect, ACS Sustainable Chem. Eng., 6 (2018) 16503–16514.

[18] S. Phanichphant, A. Nakaruk, K. Chansaenpak, D. Channei, Evaluating the photocatalytic efficiency of the $BiVO_4$/rGO photocatalyst, Sci. Rep., 9 (2019) 16091, doi: 10.1038/s41598-019-52589-5.

[19] P. Riente, M. Fianchini, P. Llanes, M.A. Pericàs, T. Noël, Shedding light on the nature of the catalytically active species in photocatalytic reactions using Bi_2O_3 semiconductor, Nat. Commun., 12 (2021) 625(1–10), doi: 10.1038/s41467-020-20882-x.

[20] M. Arumugam, M.Y. Choi, Recent progress on bismuth oxyiodide (BiOI) photocatalyst for environmental remediation, J. Ind. Eng. Chem., 81 (2020) 237–268.

[21] D. Kang, J.C. Hill, Y. Park, K.-S. Choi, Photoelectrochemical properties and photostabilities of high surface area $CuBi_2O_4$ and Ag-doped $CuBi_2O_4$ photocathodes, Chem. Mater., 28 (2016) 4331–4340.

[22] T. Arai, M. Yanagida, Y. Konishi, Y. Iwasaki, H. Sugihara, K. Sayama, Efficient complete oxidation of acetaldehyde into CO_2 over $CuBi_2O_4/WO_3$ composite photocatalyst under visible and UV light irradiation, J. Phys. Chem. C, 111 (2016) 7574–7577.

[23] L. Zhu, P. Basnet, S.R. Larson, L.P. Jones, J.Y. Howe, R.A. Tripp, Y. Zhao, Visible light-induced photoeletrochemical and antimicrobial properties of hierarchical $CuBi_2O_4$ by facile hydrothermal synthesis, ChemistrySelect, 1 (2016) 1518–1524.

[24] O.A. Arotiba, B.O. Orimolade, B.A. Koiki, Visible light–driven photoelectrocatalytic semiconductor heterojunction anodes for water treatment applications, Curr. Opin. Electrochem., 22 (2020) 25–34.

[25] Z.S. Chen, A.K.Y. Wong, T.C. Cheng, A.C. Koon, H.Y.E. Chan, FipoQ/FBXO33, a Cullin-1-based ubiquitin ligase complex component modulates ubiquitination and solubility of polyglutamine disease protein, J. Neurochem., 149 (2019) 781–798.

[26] S.P. Berglund, F.F. Abdi, P. Bogdanoff, A. Chemseddine, D. Friedrich, R.V.D. Krol, Comprehensive evaluation of $CuBi_2O_4$ as a photocathode material for photoelectrochemical water splitting, Chem. Mater., 28 (2016) 4231–4242.

[27] L. Gong, X.Y.E. Chng, Y. Du, S. Xi, B.S. Yeo, Enhanced catalysis of the electrochemical oxygen evolution reaction by iron(III) ions adsorbed on amorphous cobalt oxide, ACS Catal., 8 (2017) 807–814.

[28] F. Ambroz, T.J. Macdonald, V. Martis, I.P. Parkin, Evaluation of the BET theory for the characterization of meso and microporous MOFs, Small Methods, 2 (2018) 1800173, doi: 10.1002/smtd.201800173.

[29] Y. Wang, F. Bi, Y. Wang, M. Jia, X. Tao, Y. Jin, X. Zhang, MOF-derived CeO_2 supported Ag catalysts for toluene oxidation: the effect of synthesis method, Mol. Catal., 515 (2021) 111922, doi: 10.1016/j.mcat.2021.111922.

[30] X. Zhang, S. Xiang, Q. Du, F. Bi, K. Xie, L. Wang, Effect of calcination temperature on the structure and performance of

rod-like $MnCeO_x$ derived from MOFs catalysts, Mol. Catal., 522 (2022) 112226, doi: 10.1016/j.mcat.2022.112226.
[31] F. Soleimani, M. Salehi, A. Gholizadeh, Comparison of visible light photocatalytic degradation of different pollutants by $(Zn, Mg)_xCu_{1-x}Bi_2O_4$ nanoparticles, Ceram. Int., 45 (2019) 8926–8939.
[32] C.R. Lee, H.S. Kim, I.H. Jang, J.H. Im, N.G. Park, Pseudo-first-order adsorption kinetics of N719 dye on TiO_2 surface, ACS Appl. Mater. Interfaces, 3 (2011) 1953–1957.
[33] Z. Mao, W. Liu, H. Cai, J. Shi, Z. Wu, Y. Yang, J. Duan, A kinetic/thermodynamic study of transparent co-adsorbents and colored dye molecules in visible light based on microgravimetric quartz-crystal microbalance on porous TiO_2 films for dye-sensitized solar cells, Phys. Chem. Chem. Phys., 22 (2020) 26828–26837.
[34] F. Dong, X. Xiao, G. Jiang, Y. Zhang, W. Cui, J. Ma, Surface oxygen-vacancy induced photocatalytic activity of $La(OH)_3$ nanorods prepared by a fast and scalable method, Phys. Chem. Chem. Phys., 17 (2015) 16058–16066.
[35] H. Lahmar, M. Benamira, F.Z. Akika, M. Trari, Reduction of chromium(VI) on the hetero-system $CuBi_2O_4/TiO_2$ under solar light, J. Phys. Chem. Solids, 110 (2017) 254–259.
[36] X. Chang, T. Wang, P. Zhang, J.J. Zhang, A. Li, J.L. Gong, Enhanced surface reaction kinetics and charge separation of p-n heterojunction $Co_3O_4/BiVO_4$ photoanodes, J. Am. Chem. Soc., 137 (2015) 8356–8359.
[37] W. Zhengcui, X. Yejing, Z. Yali, L. Jingjing, C. Tao, SnS_2 nanosheet-based microstructures with high adsorption capabilities and visible light photocatalytic activities, R. Soc. Chem., 5 (2015) 24640–24648.
[38] X. Li, B. Jie, H. Lin, Z. Deng, J. Qian, Y. Yang, X. Zhang, Application of sulfate radicals-based advanced oxidation technology in degradation of trace organic contaminants (TrOCs): recent advances and prospects, J. Environ. Manage., 308 (2022) 114664(1–12), doi: 10.1016/j.jenvman.2022.114664.
[39] V.S. Lin, M. Grandbois, K. McNeill, Fluorescent molecular probes for detection of one-electron oxidants photochemically generated by dissolved organic matter, Environ. Sci. Technol., 51 (2017) 9033–9041.